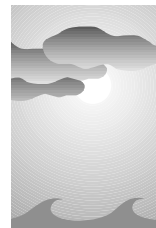# Calibration and Verification of Land Surface Temperature Anomalies Derived from the SSM/I

Claude N. Williams,* Alan Basist,* Thomas C. Peterson,* and Norman Grody+

ABSTRACT

The current network of internationally exchanged in situ station data is not distributed evenly nor densely around the globe. Consequently, the in situ data contain insufficient information to identify fine spatial structure and variations over many areas of the world. Therefore, satellite observations need to be blended with in situ data to obtain higher resolution over the global land surface. Toward this end, the authors calibrated and independently verified an algorithm that derives land surface temperatures from the Special Sensor Microwave/Imager (SSM/I). This study explains the technique used to refine a set of equations that identify various surface types and to make corresponding dynamic emissivity adjustments. This allowed estimation of the shelter height temperatures from the seven channel measurements flown on the SSM/I instrument. Data from first-order in situ stations over the eastern half of the United States were used for calibration and intersatellite adjustment. The results show that the observational difference between the in situ point measurements and the SSM/I-derived areal values is about 2°C with statistical characteristics largely independent of surface type. High-resolution monthly mean anomalies generated from the U.S. cooperative network served as independent verification over the same study area. This verification work determined that the standard deviation of the monthly mean anomalies is 0.76°C at each $1° \times 1°$ grid box. This level of accuracy is adequate to blend the SSM/I-derived temperature anomaly data with in situ data for monitoring global temperature anomalies in finer detail.

1. Introduction

For near-real-time use, global land surface temperatures and its derivative products (e.g., average global temperature time series and global temperature anomalies) have been obtained from in situ point sources located mainly within developed regions and/or near population centers. Unfortunately, these stations are neither located evenly nor densely around the globe. Great care and effort are expended in developing and maintaining these global networks. For instance, Quayle et al. (1999) developed a system that

automatically ingests the observations from the Global Historical Climate Network (GHCN; Peterson and Vose 1997) and derives the global land surface temperature from the available reporting stations. These in situ data are ingested from the Global Telecommunications System, quality assured in real time, and tested/adjusted for potential inhomogeneities. Although the GHCN currently constitutes one of the most complete datasets for historical temperature trends, it gives an inadequate spatial representation over many areas. Specifically, internationally exchanged temperature observations are sparse over large regions of Africa, tropical South America, southeastern and central Asia, and large sections of the Arctic and Antarctic.

Ancillary data such as topography and climatic characteristics have been used to interpolate the in situ stations into data-sparse regions. Although this approach results in full global coverage, the "interpolation" technique did not provide additional independent information of the global field. Furthermore, since correlation deteriorates as a function of distance from

*National Climatic Data Center, NESDIS/NOAA, Asheville, North Carolina.
+Office of Research and Applications, NESDIS/NOAA, Camp Springs, Maryland.
Corresponding author address: Claude N. Williams, National Climatic Data Center, 151 Patton Avenue, Asheville, NC 28801.
E-mail: Claude.N.Williams@noaa.gov
In final form 5 May 2000.
©2000 American Meteorological Society

the observation, interpolation has limited accuracy beyond certain distances (New et al. 2000). Such techniques may promote misrepresentation of the actual anomalies over large areas where little or no data are available. Attempts have also been made to use remotely sensed infrared observations to supplement the in situ network (Davis and Tarpley 1983; Prata and Cechet 1999). Unfortunately, clouds are opaque at infrared frequencies and difficulties with producing accurate cloud clearing algorithms increase errors over partly cloudy conditions (Ackerman 1996). In contrast, a passive microwave radiometer provides a more comprehensive way to observe the globe by directly measuring the brightness temperature from the surface under most atmospheric and surface conditions.

The observations of passive microwave radiation by polar orbiting satellites can be used to measure many of the earth's atmospheric and geophysical properties. In particular, brightness temperatures from the Special Sensor Microwave/Imager (SSM/I) have been used over land to derive surface wetness (Basist et al. 1998), snow cover (Grody and Basist 1996), surface emissivities (Prigent et al. 1997), precipitation (Ferraro and Marks 1994), and soil moisture (Vinnikov et al. 1999). Ferraro et al. (1996) give an excellent overview of numerous surface and atmospheric products developed from the SSM/I instrument. Land surface temperature has been derived having different accuracies depending on surface conditions (McFarland et al. 1990; Neale et al. 1990; Weng and Grody 1998). Basist et al. (1998) developed a technique that dynamically adjusts the SSM/I algorithm coefficients for the effect of liquid water on surface emissivity, resulting in improved temperature estimates.

The primary difficulty in deriving surface temperature from passive microwave measurements is the variable emissivity associated with different surfaces. For the microwave spectrum the emissivity of soil depends on its water and/or mineral content, as well as the effects of vegetation and surface roughness. In contrast to the microwave emissivity, the emissivity in the infrared spectrum is less dependent on the water content of the soil (Groisman and Genikhovich 1997). Since the microwave emissivity is variable, the brightness temperature is not a function of surface temperature alone. Furthermore, when snow or ice covers the surface, the upwelling radiation at low microwave frequencies primarily comes from the underlying ground (not the surface of the snow pack), while higher microwave frequencies are scattered by the ice particles (Rosenfeld and Grody 2000; Basist

et al. 1998). Unfortunately, the microwave measurements over these surfaces have little correspondence to the surface temperature and must be removed. In summary, any algorithm that attempts to estimate surface temperature must first infer the particular surface condition for a microwave measurement, filter the measurement if reliable adjustments are not currently possible, and then make appropriate emissivity adjustments to the microwave measurement if the condition indicates that the surface temperature may be derived.

It is important to remember that the SSM/I data represent an areal average of the brightness temperature of the radiating surface and not the point measurement of the ambient air temperature at shelter height. In this regard, we are comparing two essentially different physical measurements. However, in each step of this study we have striven to minimize the disparity of these datasets. It has been shown that over a given area for a given radiating surface that a comparison of the average skin temperature versus the average shelter height temperature will result in a linear relationship (Gol'tsberg 1967). The technique presented in this paper estimates the shelter height temperature directly from the SSM/I brightness temperatures using linear combinations of various terms. Implicitly, the coefficients for these linear equations include both adjustments for the emissivity of the radiating surface and corrections for the radiative transfer between the surface and the shelter height. In anomaly space the radiative transfer corrections impact the scale of the anomaly variation with respect to each surface. The separation of these corrections from the emissivity adjustments is beyond the scope of this paper.

Herein, we will describe identification of various radiating surface types, calibration of the emissivity adjustment for each unique SSM/I signature, and verification of the accuracy of our approach to estimate shelter height temperature anomalies from the passive microwave observations. Expanding on the technique implemented by McFarland et al. (1990), unique signatures of numerous surface types were identified using only the SSM/I channel measurements. Using hourly first-order stations, the emissivity adjustments were calibrated using a least absolute difference technique that minimizes the standard error for each surface type. Then, the temporal changes in these relationships were used to identify and remove intersatellite bias and intrasatellite drift. Finally, the dense U.S. cooperative network of monthly mean in situ temperature anomalies was utilized to verify the temperature anomalies derived from the SSM/I channels.

2. Data

a. SSM/I satellite data

This study uses channel measurements from the SSM/I sensors on three Defense Meteorological Satellite Program (DMSP) polar-orbiting satellites (*F08*, *F11*, and *F13*) from 1987 to 1997. The DMSP satellites provide sun synchronized overpasses at 6 A.M. and 6 P.M. These twice daily satellite overpasses are processed into $1/3° × 1/3°$ "pixels" by the National Environmental Satellite and Data Information Service and archived at the National Climatic Data Center (NCDC) in near-real time. From August 1988 to the end of 1991, erratic signals from the *F08* 85-GHz channels forced the removal of the data from our analysis. The SSM/I instrument measures the brightness temperature at four frequencies: 19, 37, and 85 GHz with vertical and horizontal polarization and 22 GHz with only vertical polarization. All of these frequencies are in atmospheric window regions with the 22- and 85-GHz channels in water vapor absorption lines, which are influenced by atmospheric water vapor and precipitable water (Weng and Grody 1998). Various signatures among the seven channel measurements were used to identify surface types and calculate dynamic emissivity adjustments. In this paper, we will distinguish between the various SSM/I channels by using the frequency in gigahertz and V for vertical and H for horizontal polarization so that the 37-GHz horizontal polarization channel will be denoted as the 37-H channel.

b. Hourly in situ data

The hourly in situ data from National Oceanic and Atmospheric Administration (NOAA) first-order stations were used to calibrate the emissivity adjustment needed to approximate the shelter height surface temperature. This dataset is primarily derived from observations made at airports, military bases, and municipal facilities that serve as primary meteorological stations. These reports are sent to NCDC, where they are quality-assured, archived, and disseminated.

c. Summary of the day in situ data

The daily maximum and minimum temperatures from the NOAA cooperative program (COOP) were used to estimate the accuracy and precision of the mean monthly anomaly series over the study period. Within the study area the COOP data come from a very dense network of volunteer observations that have undergone extensive quality assurance before the final values are archived at the NCDC.

3. Calibration of surface emissivity

a. Methodology

The eastern half of the United States was chosen for the study area. This area spans from 100°W to the eastern seaboard and from the Canadian border to the Gulf of Mexico. The complex topography of the western half of the United States excludes that region because rapid elevation changes cause large discrepancies between the point source in situ data and the areal integrated SSM/I data. Coastal areas and 70 km of their margins are excluded due to the very low emissivity of the surrounding water and the consequential noise associated with mixed signals of ocean and land. Our study area contains a moderate density of quality in situ stations with temperature measurements (Fig. 1). Over a year, the surface conditions within this region consist of wet and dry land covered by trees, grass, cities, snow, ice, and dead vegetation in a moderate elevation range (0–1600 m).

The in situ stations monitor the microclimate in a shelter 2 m above a grass surface. Tests have shown that these instruments have an accuracy of 1.0°C (Nadolski 1992) at a specific point. On the other hand, the SSM/I integrates the entire footprint (12.5–60 km) at each of the four frequencies into an average brightness temperature. The SSM/I measurements mainly emanate from the radiating surface, which can be barren and/or vegetated, though there is an atmospheric contribution at the 22- and 85-GHz water vapor frequencies. For the most accurate calibration between each SSM/I signal and the shelter height temperature at a given location, only hourly surface observations within one hour of the SSM/I overpass of the $1/3°$ square occupied by the in situ station were used. The following narration and the flowchart in Fig. 2 elucidate the methodology and procedures to simulate the shelter height temperatures from the SSM/I channel measurements.

We begin by identifying a surface type (e.g., desert, wet surface, snow cover) from the theoretical and empirical relationships among the seven channel measurements. This analysis also allows us to identify which microwave signatures (i.e., scattering, emission, and/or polarization) should be used in a regression equation to minimize the standard error between the in situ and SSM/I-derived surface temperature. The unique characteristics of each surface type are discussed in section 3b below. A regression equation for each surface type uses the unique relationship between the SSM/I channel measurements to make dynamic emissivity adjustments.
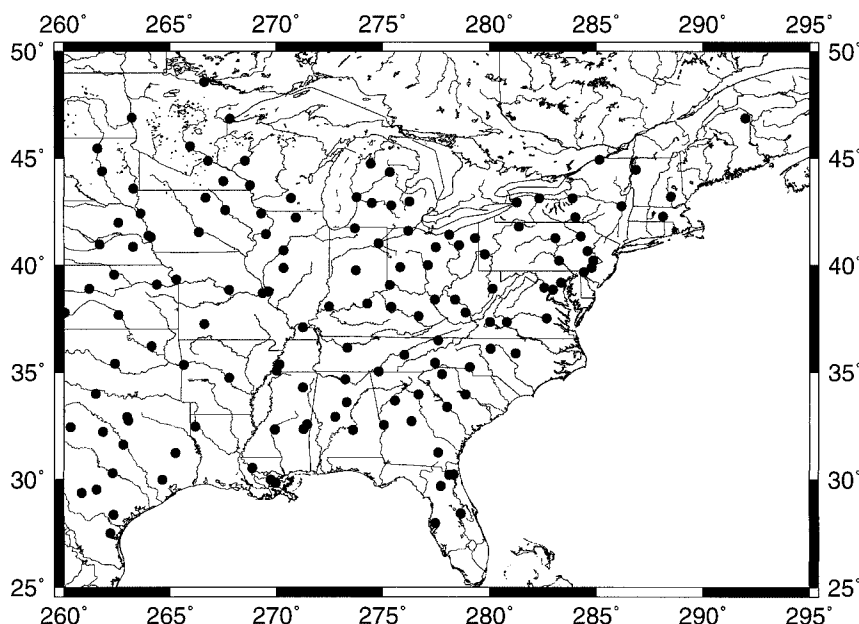
FIG. 1. The study area and the first-order stations used for calibration of the SSM/I-derived surface temperature.

Neglecting atmospheric effects, the emissivity ε_s, at a particular frequency ν, is the ratio of the brightness temperature at that frequency $T_b(\nu)$, to the actual surface temperature, T_s:

$$\varepsilon_s(\nu) = T_b(\nu)/T_s. \tag{1}$$

When the ground is dry and vegetated, the vertically polarized SSM/I channels have a nominal emissivity e_o of 0.95. However, when the surface is other than dry and vegetated, the emissivity must be implied through a function of scattering and polarization characteristics of the radiating surface. The function can be written as

$$e_s(\nu) = \beta_0 \, [f_0(\nu)] + \beta_1 \, [f_1(\nu)] + \ldots + \beta_n \, [f_n(\nu)], \tag{2}$$

where $f_0, f_1, \ldots, f_n$ are functions that contain brightness temperatures, scattering over frequency ranges, or polarization difference at given frequencies. The proportionality constants (β_0 through β_n) account for the different contributions of the various characteristics. Furthermore, the fields of view at the various frequencies range from 60 km at 19 GHz to 12.5 km at 85 GHz, and the proportionality constants in (2) partially account for this variation as well.

Substituting (2) into (1) and solving for T_s we obtain

$$T_s = T_b(\nu)/(\beta_0 \, [f_0(\nu)] + \beta_1 \, [f_1(\nu)] + \ldots + \beta_n \, [f_n(\nu)]). \tag{3}$$

It is evident that the functional form of $e_s(\nu)$ and the accuracy of T_s will improve as we learn more about the emissivity characteristics of different surfaces. Currently the specific functional form for each adjustable surface is derived from a multivariate linear regression between the SSM/I measurements and surface temperatures from the eastern half of the United States. The results of this study are more accurate than in the previous paper (Basist et al. 1998) since we have identified additional surface types to develop more precise proportionality coefficients for each classification. In using Eq. (3) to estimate shelter height temperatures from observations of the radiating surface, we rely on two critical factors. One, for a given surface there is a strong correspondence between coincident skin and shelter height temperatures (Gol'tsberg 1967). Two, the atmospheric effect is not entirely neglected because the derived coefficients, β_i, weigh heavily upon the water vapor channels (see Table 1), thereby incorporating some atmospheric contributions.

We used our past experience (Basist et al. 1998; Grody and Basist 1996; Ferraro et al. 1996) and knowledge of snow-covered, vegetated, and wet surfaces to determine the effect of physical characteristics upon the passive microwave frequencies. We then developed empirical relationships among the channels to identify and filter different surface types. A least absolute difference (LAD) algorithm (Mielke 1984) was used to obtain the best proportionality constants, β, for determining the temperature for each surface type. Differences between the derived surface temperature and the actual temperature were recursively examined to 1) further refine the proportionality constants, classification, and filtering algorithm; and 2) identify additional signals associated with new surfaces. During this process, weather maps, surface conditions, and coincident weather events were examined to identify the concurrent surface conditions within the footprint. As the task progressed, this approach led to the classification of new surface types and better proportionality coefficients relating the SSM/I channel measurements to surface temperature. It also helped

in the identification of signatures for which we cannot equate the signal from the channel measurements with in situ surface temperature. These signatures are currently viewed as indeterminate and therefore filtered [see section 3b(3)]. Any observation that failed to be identified as a specific surface type, either adjustable or unadjustable, is assumed to be in the "dry vegetated" class. As shown below, observations both in window and water vapor bands and in polarization are key to our ability to identify surface types and estimate emissivity.

Hourly temperature measurements from the first-order network were compared to the corresponding SSM/I-derived temperature at the time of the DMSP satellite overpass. The SSM/I channel measurements for these comparisons came from the descending (morning) pass of the *F11* satellite because this satellite has the most stable orbit of the three satellites (see section 4) and the near surface boundary layer temperature approaches equilibrium with the skin temperature in the early morning (Betts and Ball 1995).

b. Results of emissivity calibration

1) FILTERS FOR ADJUSTABLE SURFACES

The inset in each of the graphs in Fig. 3 illustrates the unique empirical relationships among the channels used to identify and filter each surface type. This is a simplified signature of brightness temperature versus frequency. The "dry vegetated" signature (Fig. 3a) shows that emissivity goes up slightly with frequency, and that there is a slightly greater increase in emissivity for the horizontal compared to the vertical polarization, that is to say, the polarization difference decreases as frequency rises.

The next three surfaces (Figs. 3b–d) illustrate how liquid water affects the different SSM/I channels to form distinct signatures. The simplified signature of a "wet surface," shown in Fig. 3b, shows that emissivity increases rather quickly with frequency. Furthermore, polarization differences for wet surfaces rapidly decrease as the frequency increases. The simplified signature of "light rain" (Fig. 3c) illustrates a pattern very similar to that of a wet surface. However, the scattering and polarization difference characteristics change as frequency increases, resulting in a separate surface to be filtered and adjusted. The simplified signature for "moderate rain" (Fig. 3d) indicates that the emissivity increases with frequency at the lower frequencies (19, 22, 37 GHz) but decreases at the highest frequency of 85 GHz. This behavior corresponds to ice scattering at high frequencies due to precipita-
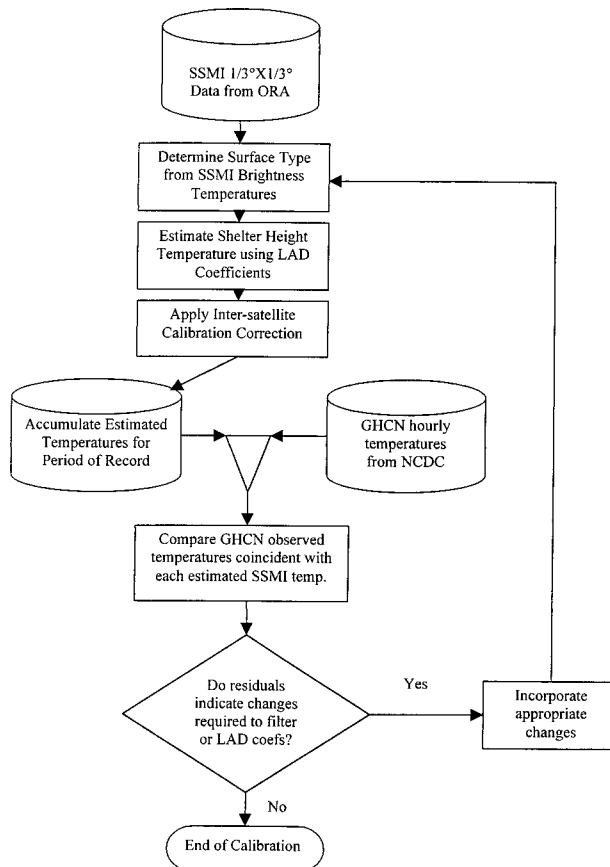

FIG. 2. Flowchart describing the procedure to simulate the shelter height temperatures from the SSM/I channel measurements.

tion, while the low frequencies respond to the emissivity of wet surfaces.

The "thin fresh snow cover" surface (Fig. 3e) is the best snow-cover surface for attempting to derive surface temperature at the SSM/I frequencies. The decline in emissivity at the high frequencies due to the scattering from the snow grains is characteristic of all snow surfaces. However, a low polarization difference at 19 GHz and the monotonic decrease of brightness temperature with frequency corresponds to shallow snow that has not undergone any metamorphosis (Rosenfeld and Grody 2000).

The distinct signature for "calcic soil" (Fig. 3f) shows that the brightness temperature is lower for the 19- and 37-GHz window channels compared to the 22- and 85-GHz channels that contain a small atmospheric water vapor contribution. This is due to the low emissivity of calcic (limestone) material, which results in an increase of the upwelling radiation for the water vapor channels relative to the more transparent window channels. For this surface, the polarization difference only decreases moderately as the frequency increases.

TABLE 1. The various surfaces for which emissivity adjustments have been determined using the LAD algorithm. The corresponding parameters and coefficients defined in Eq. (3) are listed along with statistical measures of the goodness of fit of the residual in situ minus SSM/I values.

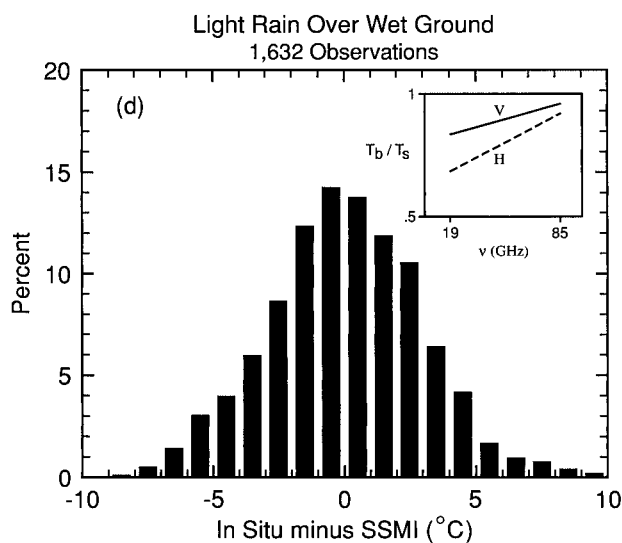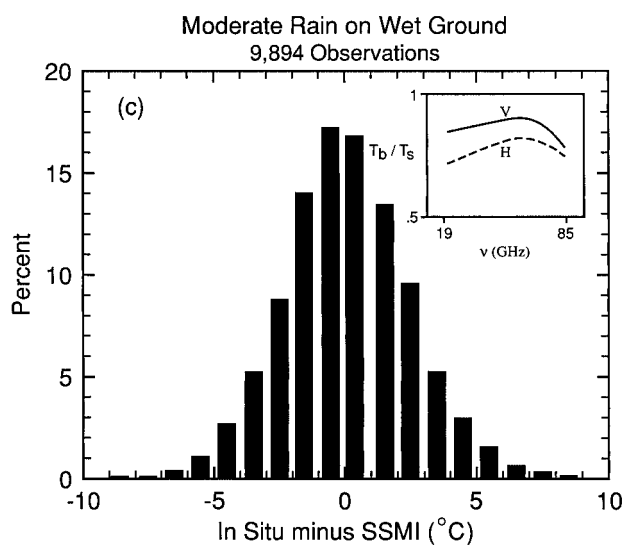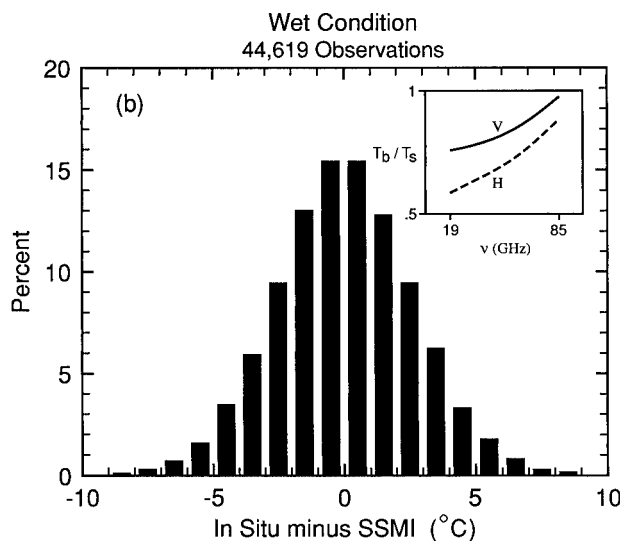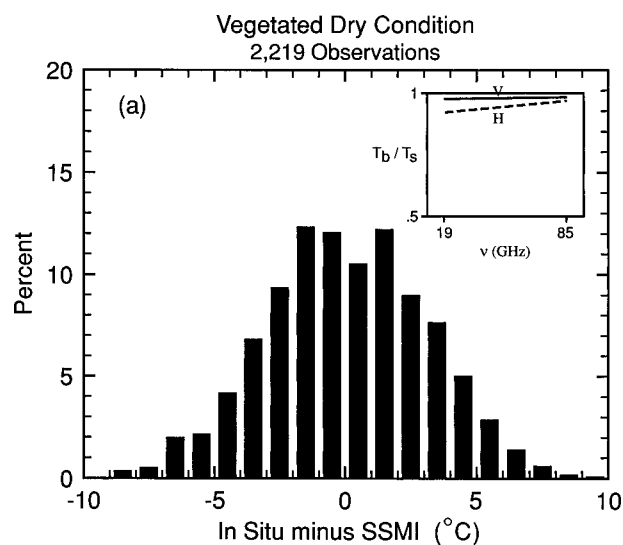|	Vegetated dry land	Wet surface	Light rain on wet surface	Moderate rain on wet surface	Limestone	Fresh snow
First parameter coefficient	22V $\beta = 1.065$	85V $\beta = 1.454$	22V $\beta = 1.071$	22V $\beta = 1.056$	22V $\beta = 2.314$	22V $\beta = 1.064$
Second parameter coefficient	—	22V − 19V $\beta = -0.134$	22V − 85V $\beta = 0.218$	19V − 19H $\beta = 0.320$	37V $\beta = -2.11$	22V − 37V $\beta = 0.169$
Third parameter coefficient	—	37H $\beta = -0.405$	—	37V − 85V $\beta = -0.501$	85V $\beta = 0.846$	—
Fourth parameter coefficient	—	85V − 37V $\beta = -0.784$	—	—	—	—
No. observations	2219	44 619	2882	9894	4883	1597
Average error	0.061°C	0.021°C	0.033°C	0.052°C	0.180°C	−0.218°C
Standard deviation	3.144°C	2.64°C	2.914°C	2.416°C	4.286°C	3.874°C
Skewness	−0.006	0.066	−0.031	0.090	0.494	−0.219
Kurtosis	0.071	0.502	0.370	0.414	2.599	0.260

2) RESIDUALS OF ADJUSTABLE SURFACES

As stated previously, over most dry vegetated surfaces the assumed background emissivity, e_o, is 0.95 at 22V with very little change at other frequencies (Basist et al. 1998), so that $T_s \cong T_b(22V)/e_o(22V)$. From the LAD algorithm, the lowest residual relationship between T_s and T_b for this surface is achieved with a proportionality coefficient of 1.065 when using the 22V SSM/I channel. Since the empirically derived proportionality constant for a dry vegetated surface is very close to the theoretically determined value (i.e., $\beta_0 = 1.0/e_o$), our initial technique for calculating surface temperature is very accurate. The histogram of the differences between concurrent in situ and SSM/I surface measurements for the dry vegetated surface is shown in Fig. 3a. The LAD residuals (in situ minus SSM/I) form a symmetrical distribution that is slightly flattened around zero (0) difference. This may indicate that multiple signatures are passing through the filter and that further study could discriminate and separate the signals into several, better estimated, conditions. The standard deviation of the residuals (from Table 1) is the highest of the first four surfaces that are symmetrical and tightly bunched around the mean.

The next three surfaces display our ability to estimate the surface temperature for different surface conditions pertaining to wet surfaces and rain. The wet surface (Fig. 3b) with more than 44 000 data points, has by far the largest number of observations for any surface type in the study. This surface condition is a refinement of the wet SSM/I signatures used to develop the algorithms in Basist et al. (1998). It has an extremely well defined filter and uses four parameters to estimate surface temperature (Table 1). The majority of the weight resides in the 85V channel measurement because of the higher emissivity of water (which reduces its effect) at the higher frequencies. The distribution of the LAD residuals is peaked at zero (0)

FIG. 3 (*facing page*). A histogram of the differences between in situ and SSM/I surface temperatures for various surface conditions (a–f) over the eastern United States. The upper-right corner of each figure provides an idealized depiction of the SSM/I spectral signature for that surface.

Vegetated Dry Condition
2,219 Observations

Wet Condition
44,619 Observations

Moderate Rain on Wet Ground
9,894 Observations

Light Rain Over Wet Ground
1,632 Observations

Snow Condition
1,597 Observations

Limestone Surface
197 Observations
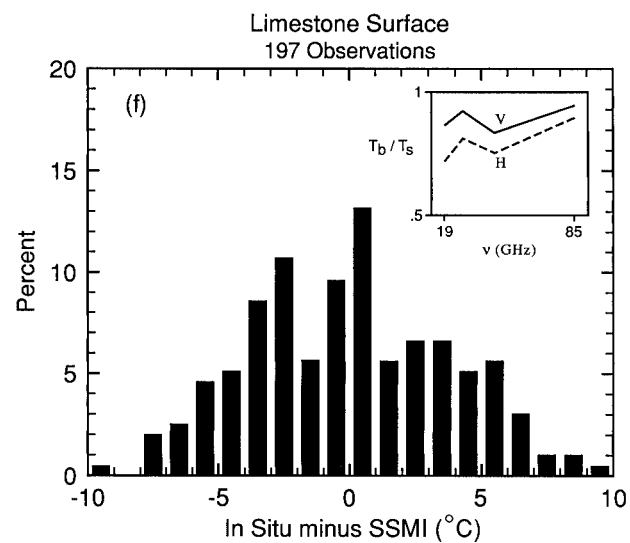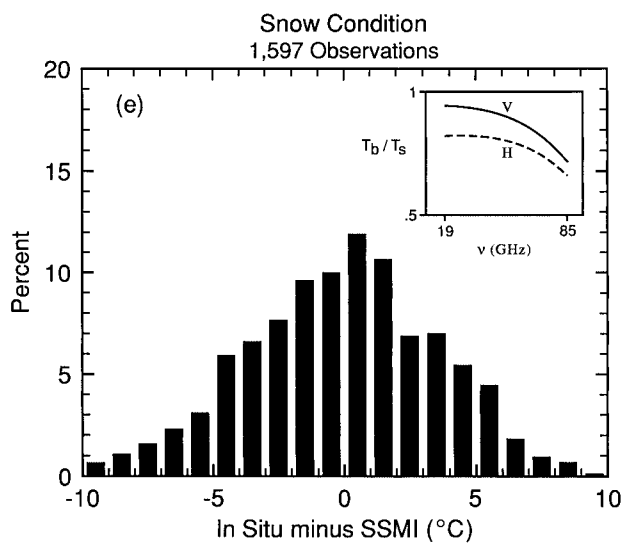
difference, highly symmetrical, and the second lowest standard deviation of the adjustable conditions. The residuals for light rain (Fig. 3d) and moderate rain (Fig. 3c) are very similar to that of the wet surface. The major factors that separate these three surface conditions are the filters needed to selectively identify each and the parameters necessary to most accurately estimate surface temperature.

The difference between in situ and SSM/I surface measurements for a thin fresh snow-cover surface is shown in Fig. 3e. With a flattened, asymmetrical distribution, this is the only one of many snow surfaces that could offer derived surface temperatures at SSM/I frequencies. More work and ancillary data are needed to improve this surface.

Even with a very distinct signature, the calcic soil surface (Fig. 3f) has very few observations in the study region and represents the highest variance of all the acceptable surfaces. Due to the lack of exposed limestone in the study area, we were forced to use locations in the western United States. Consequently, topography and a limited number of concurrent measurements added more noise to the regression. We are trying to obtain hourly temperatures over Australia where limestone is exposed and topography does not play a major role. Our hope is to reduce the residuals with such data.

3) UNADJUSTABLE SURFACE CONDITIONS

It is important to remove the surface-temperature estimates from most snow- and ice-covered surfaces. First, the microwave signals from these bodies radiate from the underlying surface. Since snow is an effective insulator, this makes the signal sensed by the SSM/I unrelated to the near-surface air temperature. The second reason is that once the ice grains have undergone any significant metamorphic process, such as freeze/thaw cycles or firnafication in a deep snow pack, the grain size increases and changes the microwave scattering characteristics. Therefore, we restrict our adjustment for snow cover to freshly fallen and relatively thin snow packs by using scattering characteristics at the lower and higher SSM/I frequencies to filter deep snow and snow that has undergone metamorphosis into other forms of ice.

Water on the surface reduces the emissivity and increases the polarization difference at all SSM/I frequencies. Theoretical and empirical evidence indicates that the emissivity reduction is a nonlinear function of the brightness temperature, although a linear assumption is reasonable when the ratio of water to land/vegetation stays below a certain threshold (Basist et al. 1998). As the amount of water on the surface increases, emissivity decreases so much that atmospheric water vapor as well as other factors not addressed in our analysis become major sources of noise because the surface signal-to-emissivity ratio becomes so low. The acceptable threshold of the ratio of dry to wet surfaces varies as a function of the emitting surface and atmospheric conditions. For instance, on the tundra, where the atmospheric moisture is low and the surface is riddled with small pools of water, we have found that the linear assumption is valid up to as much as 50% water. However, where the land is a combination of lake and dry ground and atmospheric moisture is high, the linear assumption is only reliable where less than 30% of the surface is covered by water.

The "mixed pixel" condition removes all the SSM/I observations with irregular changes in the signal associated with spatial inhomogeneity within the footprint. As an illustration, near the coast the 85-GHz measurement (12.5-km diameter) may represent dry ground, whereas at 19 GHz (60-km diameter) the signal may be depressed due to the contributions of water bodies within the large footprint. Another category filtered from the analyses is "bad" observations, which occurs when there are either instrument or processing problems. These types of observations register variations between adjacent frequencies of 30°C or more, yield a horizontal polarization measurement higher than the vertical polarization measurement, or measure brightness temperatures greater than 150°C or less than −120°C in one or more channels.

4. Intersatellite calibration

a. Methodology for the intersatellite calibration

The algorithms described in the preceding section were developed using the *F11* 6 A.M. data. To apply these algorithms to the 6 A.M. and 6 P.M. data of all the satellites, we chose a linear regression analysis of the mean monthly temperature anomaly fields. Monthly anomalies were chosen because seasonal changes in the diurnal cycle strongly affect the relationship between monthly average temperatures computed using daily maximum and minimum compared to fixed hour (e.g., 6 A.M. and 6 P.M.) observations. To examine this impact, we generated monthly anomalies for both methods using the hourly first-order stations within the study region for all the months in the period of record.

A histogram of the anomalies (Fig. 4) shows that the time of observation bias in the diurnal cycle is removed using monthly average anomalies. Figure 4 also shows the distribution of the differences between these methods as peaked and symmetrical around zero with a standard deviation of 0.096°C. There is also evidence that the instrument's exposure to sunlight and the position of the heat-regulating louvers may also induce a spurious interannual component to the brightness temperatures (Christy et al. 1998).

The linear regression analysis addresses three known influences: 1) changes in overpass time make the temperature trend dependent on the annual cycle and latitude, 2) linear deterioration of the sensor or calibration equipment, and 3) decrease in the altitude of the satellite. The simple methodology is illustrated by a flowchart in Fig. 5. Separate sets of linear coefficients identify the drifts for morning and afternoon passes on each satellite (see Table 2).

b. Results of the intersatellite calibration

The difference between the eastern U.S. mean monthly anomalies for the morning and afternoon passes of the *F08*, *F11*, and *F13* and the corresponding anomalies for the coincident in situ observations are plotted in Fig. 6. This plot illustrates how the drift characteristic of each satellite is unique. Superimposed on each of these slopes is unexplained noise that may be caused by errors in the satellite-derived product and/or variations in the boundary conditions that influence the relationship between in situ shelter height and satellite-derived temperatures.
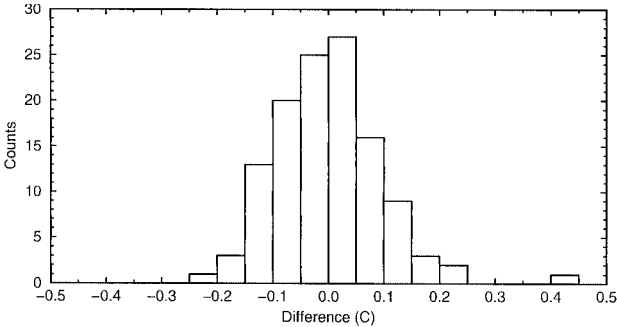

FIG. 4. The difference between the mean monthly anomalies calculated by different methods using the hourly first-order stations. The first method is the average of the daily maximum and minimum temperatures. The second method is the average of the 6 A.M. and 6 P.M. temperatures.

Once the linear regression lines are removed, the morning and afternoon curves are averaged together for each satellite. Figure 7 shows a time series of all three satellites with the linear regression fits removed. These residuals are small compared to the size of the regional anomalies and will be removed with an active in situ anchor in our final blended product.

5. Verification with high-density in situ data

a. Methodology of the verification

Up to this point we have been directly comparing the individual observations from the SSM/I and hourly data. This approach ensured the most accurate propor-

TABLE 2. Linear regression coefficients for the intersatellite calibration (ISC) calculated for the morning and afternoon overpasses of each satellite used in the study. The ISC calculated from this table produce the monthly offsets removed from Fig. 6 to generate Fig. 7.

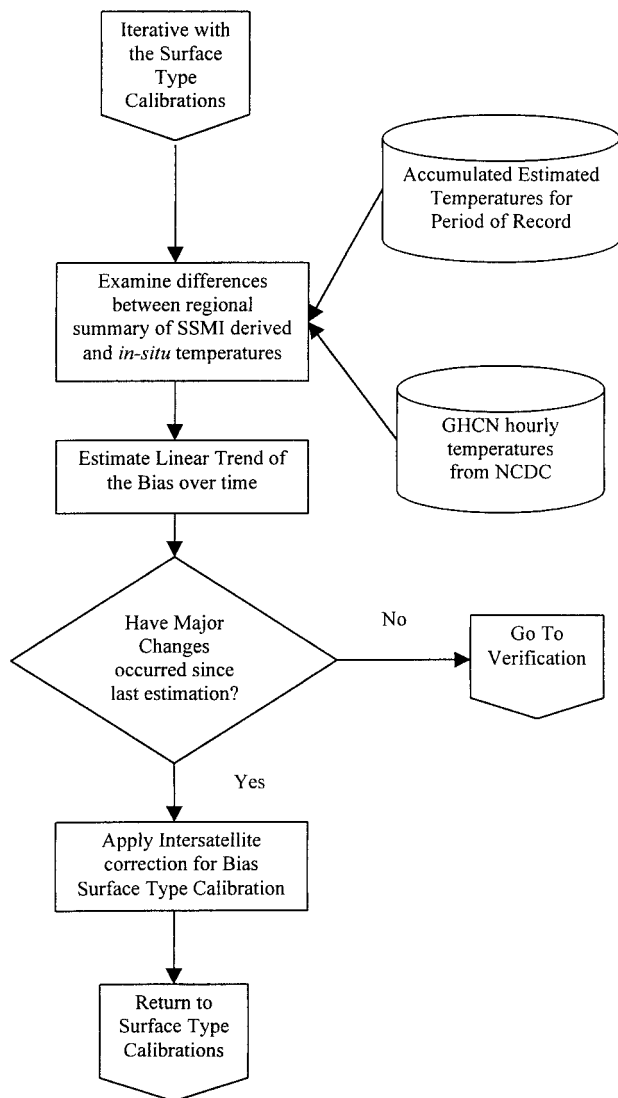| Hour	Node	Satellite	Slope (°C)	Intercept (°C)	Begin year	Begin month	End year	End month
06	as	*F08*	−0.297	1.344	1987	Jul	1990	Jul
06	ds	*F11*	0.060	−0.168	1992	Jan	1995	Apr
06	ds	*F13*	−0.294	0.623	1995	May	9999	Jan
18	ds	*F08*	−0.728	5.750	1987	Jul	1990	Jul
18	as	*F11*	0.546	1.039	1992	Jan	1995	Apr
18	as	*F13*	−0.616	3.099	1995	May	9999	Jan

FIG. 5. A flowchart of the procedure to account for and remove the intersatellite drifts for all three microwave instruments.
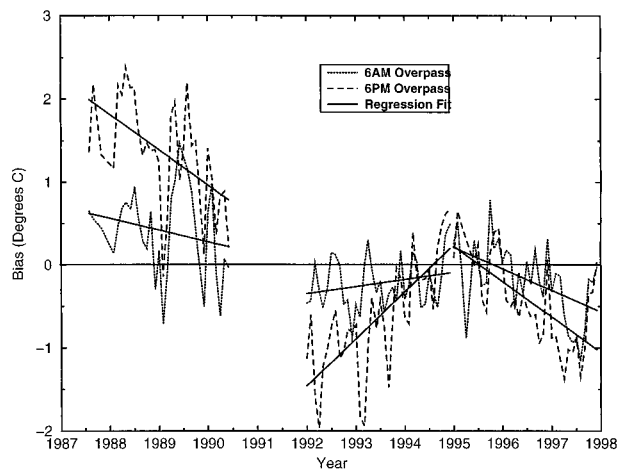

FIG. 6. The bias between in situ and SSM/I-derived temperature anomalies during the morning and afternoon passes of the *F08* (1987–90), *F11* (1992–94), and *F13* (1995–97), independently. This diagram illustrates that the drift characteristic of each satellite is unique.

which monthly anomalies are calculated. This high-resolution dataset in the United States is an excellent verification dataset to test the ability of the satellite anomalies to monitor regional monthly temperature anomalies.

The verification region is the same region used in the calibration study, encompassing the eastern half of the United States from the Canadian border to the Gulf of Mexico, and from 100°W to the East Coast. Each 1° × 1° grid box over this land surface area contains between 6 and 13 in situ stations. In contrast, the average brightness temperature from the SSM/I measurement integrates up to nine derived temperatures in each 1° × 1° grid box.

The SSM/I channel measurements were processed through our currently "best" surface filtering and emissivity adjustment algorithms to obtain the derived 6 A.M. and 6 P.M. temperature daily observations. For each 1/3° pixel the SSM/I-derived daily observations were tested against filters described in the succeeding paragraphs. Even with our best estimations of surface temperature from the SSM/I data, orbital gaps limit coverage in the mid- and low latitudes. Data dropouts and our filters also limit the satellite-derived coverage such that extreme care must be taken to represent a month's anomalies with the remaining observations. The most damaging effect is caused by the inability to derive surface temperatures during snow events. A persistent snow cover of a few days can cause a significant warm bias in the mean monthly anomalies. Several filters attempt to limit this effect.
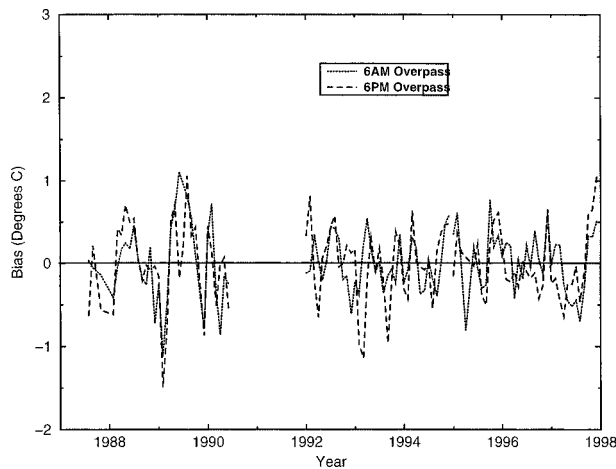
tionality constants for the emissivity adjustments and the best regression coefficients for the intersatellite calibrations. Our next goal is to test the accuracy and precision of the SSM/I-derived temperature anomalies against independent in situ data–based monthly anomalies. Figure 8 illustrates the process used to compare the SSM/I-derived anomalies with the verification dataset anomalies. We used the dense cooperative network of daily maximum and minimum temperatures to derive an in situ mean monthly anomaly series from 1987 to 1997. All of the days with both maximum and minimum temperature observations were averaged for each day, then these daily values were averaged into monthly mean values from

FIG. 7. Same as Fig. 6, after the linear drifts are removed.

The following "runs" test is a filter to remove months without enough daily SSM/I observations to adequately represent the monthly in situ value. If three periods of five consecutive days, or two periods of six consecutive days, or one period of seven consecutive days are missing, then the monthly satellite-derived temperature for the 1/3° pixel is defined as missing. Similarly, the monthly temperature was set to missing if five consecutive days of snow cover or snow-cover observations bracketing missing values were observed. If a month was not removed after passing through these filters, temporal interpolation schemes from none at all to cubic spline with various tensions were investigated before we identified that a linear approach provided the best procedure to fill in the remaining missing days before calculating the monthly temperature in the remaining 1/3° pixels.

We performed a preliminary study to identify how the statistical distribution of point and areal averaged measurements represent their respective grand anomaly in each 1° × 1° grid box. Figure 9 illustrates the absolute difference and variation of the average of individual anomalies in larger and larger groups compared to the grand mean. A single station or pixel value has an average absolute difference of 1°C compared to the grid box mean and a standard deviation of 1°C about this difference. The absolute difference and variation of both datasets diminish asymptotically toward zero as the number of values averaged together increases. By the time three values within a grid box are averaged together, the absolute difference diminishes to 0.5°C, with a variation of around 0.5°C. This point offered a compromise between removing too many grid boxes due to insufficient data and restrict-
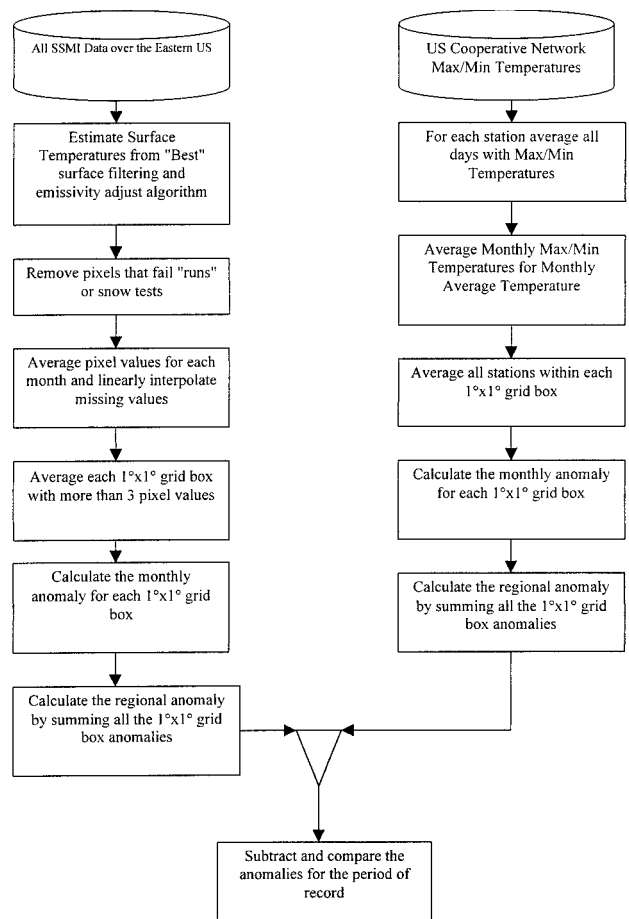

FIG. 8. Flowchart of the process used to compare the SSM/I-derived mean monthly anomalies with the cooperative network dataset anomalies.
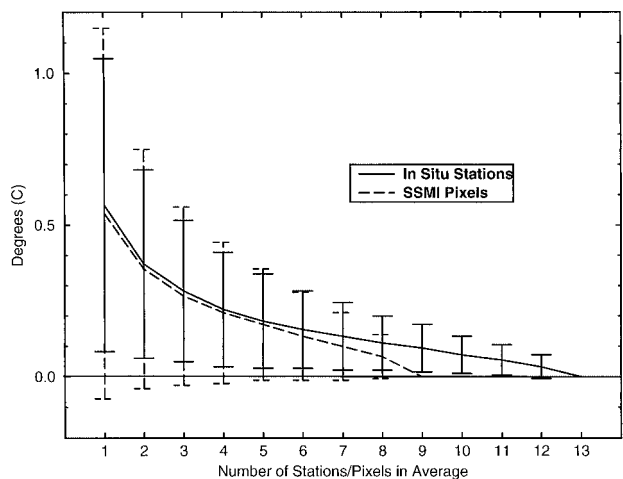

FIG. 9. Plot showing the ability of both an in situ observation and SSM/I pixel to represent their corresponding mean anomaly from a 1° × 1° grid box. The plot starts out comparing individual values against the grid box mean and their standard deviation. The following values represent the error characteristics as more observations are averaged together to represent the grid box mean.
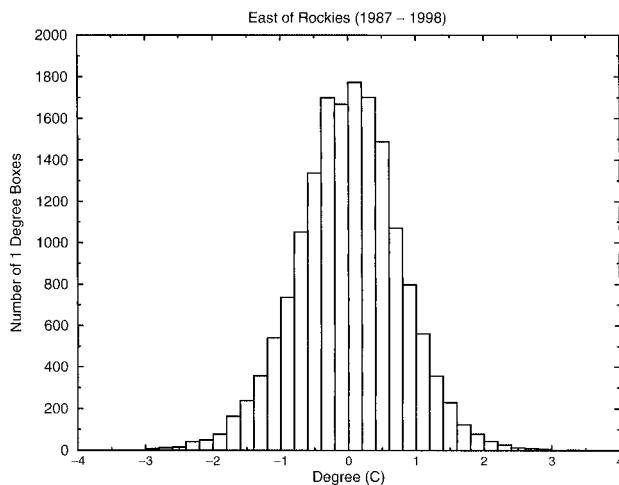
FIG. 10. Distribution of the residuals between each $1° \times 1°$ grid of in situ minus SSM/I monthly temperature anomalies. Each monthly grid box value is a separate observation providing more than 10 000 data points over the study period.
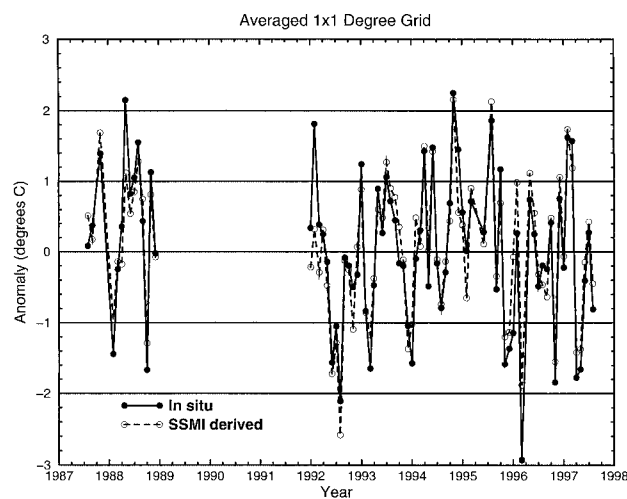

FIG. 11. Time series of monthly anomalies across the study area over the period 1987–97, with a period between 1989 and 1991 removed (as discussed in the text). Anomalies during the record generally fluctuate between −2° and 2°C, with average fluctuation from the mean averaging 1.15°C.
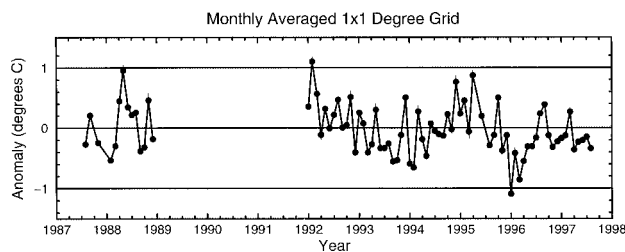

FIG. 12. Time series on the difference between the two datasets presented in Fig. 11.

ing the uncertainty of the calculated grid box mean. So that once the 1/3° resolution data has passed through the preceding filters, at least three out of the nine pixels must have values before an average value is calculated to represent the 1° grid box.

Next, a histogram of the monthly differences between the two anomaly fields at each grid box shows the correspondence between in situ– and satellite-based anomalies for the entire region and period of record. To test the ability of the satellite-derived anomalies to represent the in situ–based anomalies in the corresponding grid box, the individual monthly mean anomalies for each dataset were calculated independently. These series were compared for the period of record. Various statistics identify the correspondence and deviations in these two fields. Last, spatial auto-correlation and/or temporal correlation for each $1° \times 1°$ grid box throughout the study area is calculated and graphically presented in a map format.

Improvements to the generation of $1° \times 1°$ temperature anomalies with respect to the warm snow bias and the linear interpolation technique for better agreement with in situ measurements can be found in Peterson et al. (2000).

b. Results of the verification

Figure 10 shows the distribution of the residuals of in situ minus satellite-derived monthly temperature anomalies for all remaining $1° \times 1°$ grids. This analysis of more than 10 000 data points with a standard deviation of 0.76°C indicates that the satellite-derived monthly temperature anomalies have a strong correspondence to the in situ–based anomaly. It is important to note that these differences can be ascribed to several factors: errors in the derived temperatures, in situ measurement errors, variations in atmospheric contributions, differences between point measurements and spatially integrated values, and discrepancies between shelter height temperature anomalies and those at the radiating surface. An analysis of the spatial structure in the satellite-derived field consistently demonstrates strong coherence well within 0.5°C.

The time series of monthly anomalies across the study area over the period 1987–97, with a period between 1989 and 1991 removed (as discussed above) is presented in Fig. 11. The regional anomalies generally fluctuate between −2° and 2°C and the average fluctuation from the mean is 1.15°C. The two datasets share the variance with a signal-to-noise ratio of 2.5 and a mean difference of 0.34°C. The correlation coefficient (r) over the time series is 0.92. Figure 12

shows a time series of the difference between the two datasets. There are two occasions when the differences exceed 1°C. These are winter months when the sampling is greatly diminished in the study area due to snow. During almost every month the differences were far less than the actual temperature anomaly.

The temporal correlation in each grid box of the study area is mapped in Fig. 13. There is a significant area where the correlation coefficient (r) exceeds 0.90. This area covers portions of the northern plains, the Midwest, and the Tennessee valley. The majority of the study area has correlation coefficients greater than 0.80, which means that more than two-thirds of the variance is shared between the in situ and satellite-derived temperature anomalies. There are some limited areas where correlation coefficients drop below 0.70. One of these areas is eastern Texas, where we have investigated potential causes for the lower correlation over this area and have not been able to identify any particular source of the problem. Another area with a lower correlation is the lower Mississippi valley. This area experiences extreme flooding during part of the year. When there is extensive surface water, the relationship between channel measurements becomes non-linear and introduces noise in the derived product. In general, the two fields have both high spatial and temporal correlation throughout the study.

6. Summary and conclusions

In situ temperature observations do not provide finely detailed global coverage; therefore, additional data sources are needed to supplement these traditional observations. Satellite-borne infrared observations have been tried for years, but cloud contamination continues to resist filtering. This leaves passive microwave radiation as the next best option. Although clouds are not a problem in the microwave spectrum, there is the issue of variable emissivity of the radiating surface. We addressed this

variation by understanding the radiating characteristics of numerous surfaces and made dynamic emissivity adjustments as a consequence of the surface type of each observed signal.

Spatially and temporally coincident SSM/I observations and in situ data were used to develop regression equations to estimate the emissivity adjustments. Each adjustable surface type within the SSM/I data has a different set of parameters and goodness of fit with respect to the shelter height temperatures. The intersatellite calibration expanded the usable SSM/I observations to include all of the 6 A.M. and 6 P.M. satellites by correcting for linear nonmeteorological changes in the signals over time, for example, changes in satellite, drifts in overpass time, sensor drift, and altitude reduction.

An independent high-resolution dataset was used to validate the accuracy and precision of the satellite-derived surface temperature anomalies. Both the satellite and reference time series had similar distributions around their mean, and the difference between the two anomaly fields had a standard deviation of 0.76°C with low kurtosis and skewness. The spatial correlation over
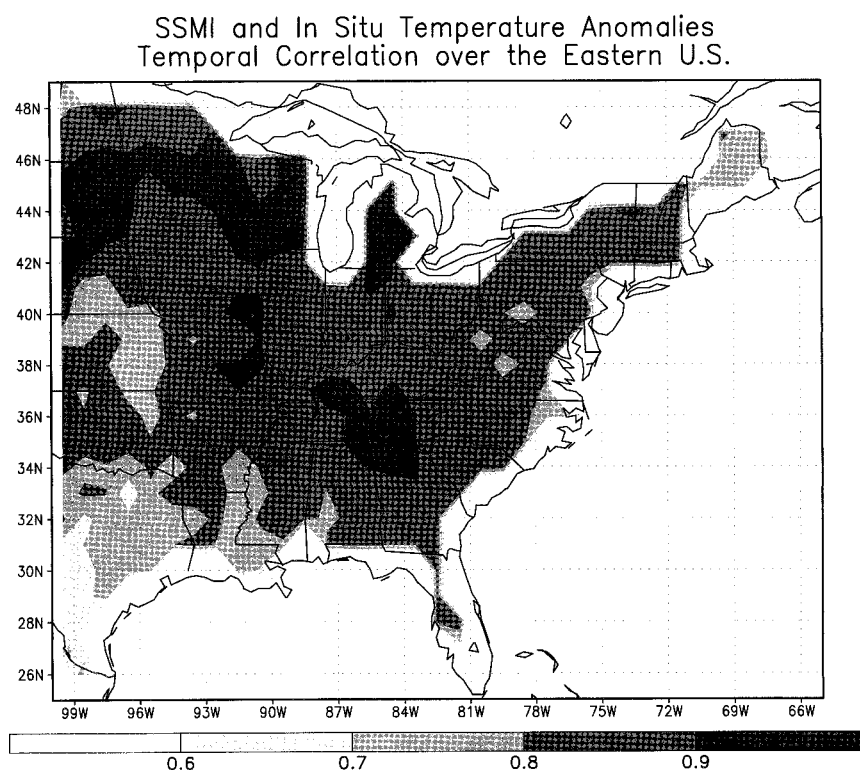

FIG. 13. Temporal correlation in each grid box of the study area. There is a significant area where the correlation coefficient exceeds 0.90; this area covers portions of the northern plains, the Midwest, and the Tennessee valley. The majority of the study area has correlation coefficients greater than 0.80, although some isolated areas do drop below 0.70.

the time series was 0.92 and temporal correlation over the study area generally exceeded 0.80. There was some spatial and temporal autocorrelation in the residual, but it is at an acceptable level.

Several limitations to be corrected in future work are worth noting. Expansion of the SSM/I measurements to fill in orbital gaps, data dropouts, and missing days will generate a more representative monthly time series. Examination of in situ data from other regions will help determine the effects of the diurnal cycle. It is planned to 1) include data from other SSM/I satellite platforms at different overpass times, 2) identify a new base period and perform similar analyses to the ones presented in this study, 3) add many satellite orbits that are missing in our current datasets, and 4) investigate changes in the diurnal cycle related to location and latitude. To improve the derived temperature over barren surfaces, daily in situ observations from Australia and elsewhere may remove current topography problems. Also, the utility of infrared data will be studied for temperatures over snow-covered areas and barren surfaces. Introduction of new surface-type categories and investigation of nonlinear relationships between SSM/I channel measurements and

emissivity, along with adjustments to incorporate currently unusable data, will improve temperature derivations for the existing categories.

Even with the shortcomings mentioned in the preceding paragraph and the necessity to refine limestone and other barren surface types, we scrutinized the ability of this technique to derive land surface temperature anomalies on a global scale. A representative comparison of the SSM/I-derived temperature anomalies with the NOAA sea surface temperature anomalies (Reynolds and Smith 1994) is shown for June 1998 (Fig. 14). This map is a composite of the monthly $1° \times 1°$ temperature anomalies for both datasets using the 1992–98 base period. Note the correspondence and continuity of the two independent datasets as coastal anomalies smoothly merge together and the strong wave structure across the northern tier of the Northern Hemisphere. In areas where the land–ocean temperature relationship is weak, such as the Arabian peninsula, Queensland, western North America, and southeast Asia, there is excellent agreement between the GHCN (Fig. 15) and SSM/I anomalies. In areas where the GHCN has full coverage, such as the United States and Europe, the SSM/I dataset reveals much
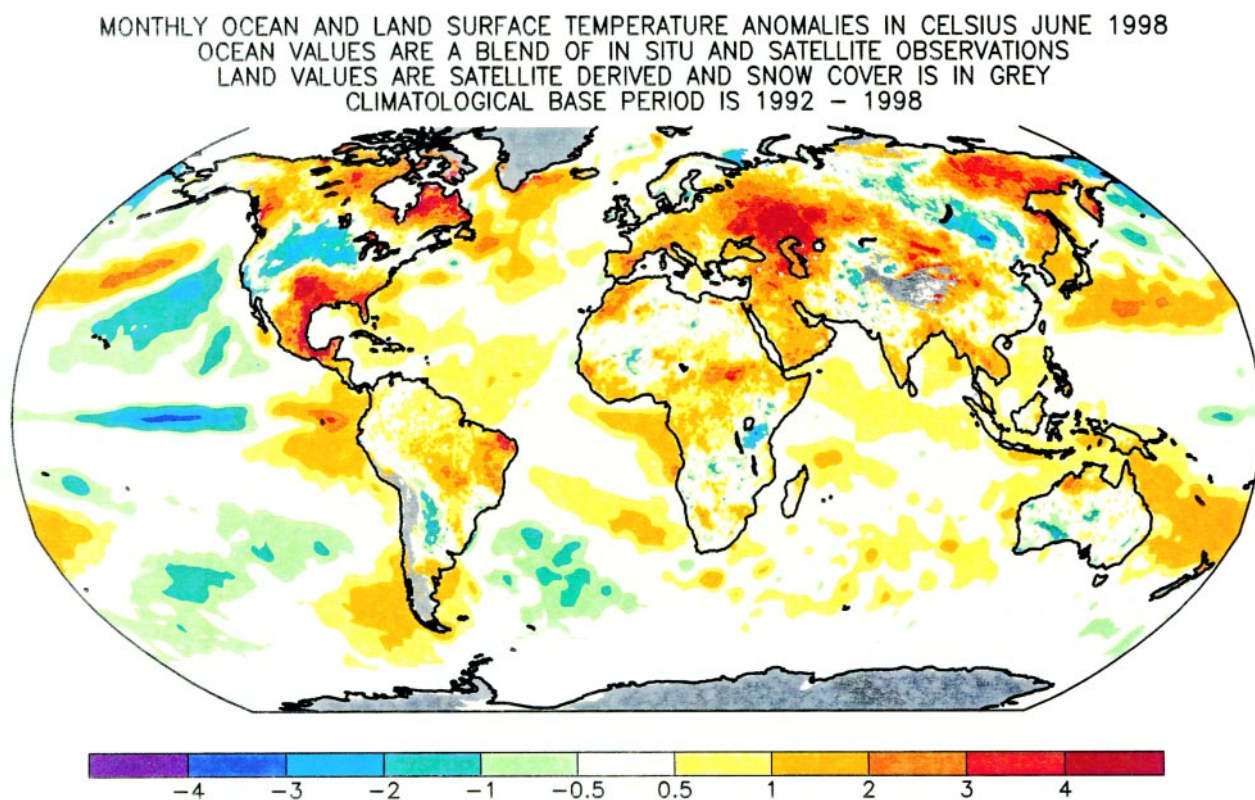

FIG. 14. Map of global surface temperature anomalies provided from the SSM/I instrument and NOAA-blended SST product during June 1998, using a 1992–98 base period. Anomalies are derived at 1°C resolution.

finer detail. In GHCN data-sparse regions, such as western and northern Asia, central Africa, and South America, the greater coverage and finer resolution of the SSM/I reveals anomaly patterns unavailable through the in situ network. Finally, the anomalies over Australia (where limestone and quartz prevail) have an excellent correspondence between the two datasets. The point is that the global relationship between a high quality network like the GHCN and the SSM/I-derived temperature anomalies is strong and will only improve as better filtering algorithms and calibration coefficients are derived over such surfaces. A comprehensive analysis of a global blended product using the SSM/I-derived and GHCN temperatures is described in the companion article by Peterson et al. (2000).

Although we categorized and adjusted emissivity of many surface types to produce a finely detailed land surface temperature anomaly field, this is a continuing process, and further studies are needed to develop ways to merge other remotely sensed observations and to better understand the relationship between the SSM/I channel measurements and in situ temperatures.

References

Ackerman, S., 1996: Global satellite observations of negative brightness temperature differences between 11 and 6.7. *J. Atmos. Sci.,* **53,** 2803–2812.

Basist, A. N., N. C. Grody, T. C. Peterson, and C. N. Williams, 1998: Using the Special Sensor Microwave/Imager to monitor land surface temperature, wetness, and snow cover. *J. Appl. Meteor.,* **37,** 888–911.

Betts, A. K., and J. H. Ball, 1995: The FIFE surface diurnal cycle climate. *J. Geophys. Res.,* **100,** 25 679–25 693.

Christy, J. R., R. Spencer, and W. D. Braswell, 2000: MSU tropospheric temperatures: Dataset construction and radiosonde comparisons. *J. Atmos. Oceanic Technol.,* in press.

Davis, P. A., and J. D. Tarpley, 1983: Estimation of shelter temperatures from operational satellite sounder data. *J. Climate Appl. Meteor.,* **22,** 369–376.

Ferraro, R. R., and G. F. Marks, 1994: Effects of surface conditions on rain identification using the SSM/I. *Remote Sens. Rev.,* **11,** 195–209.
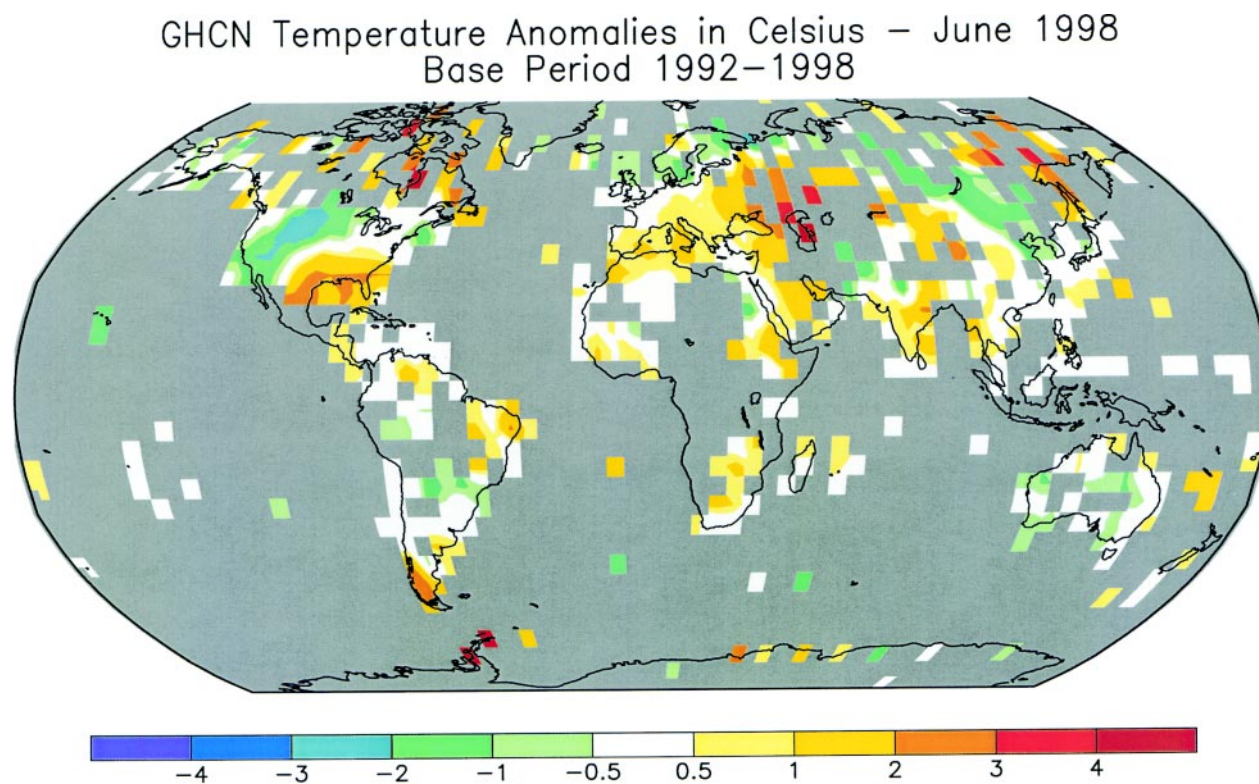
FIG. 15. The GHCN surface temperature anomalies for the same base period as Fig. 14. Comparison of the land surface temperature anomalies between the SSM/I derived and the GHCN show excellent agreement globally.

——, F. Weng, N. C. Grody, and A. N. Basist, 1996: An eight-year (1987–1994) time series of rainfall, clouds, water vapor, snow cover, sea ice derived from SSM/I measurements. *Bull. Amer. Meteor. Soc.,* **77,** 891–905.

Gol'tsberg, I. A., Ed., 1967: Heat regime of the active surface. *Microclimate of the USSR,* Israel Program for Scientific Translations, 62–91.

Grody, N. C., and A. Basist, 1996: Global identification of snow cover using SSM/I measurements. *IEEE Trans. Geosci. Remote Sens.,* **34,** 237–249.

Groisman, P. Y., and F. L. Genikhovich, 1997: Assessing surface–atmosphere interactions using former Soviet Union standard meteorological network data. Part I: Methods. *J. Climate,* **10,** 2154–2183.

McFarland, J. M., R. L. Miller, and C. M. U. Neale, 1990: Land surface temperature derived from the SSM/I passive microwave brightness temperatures. *IEEE Trans. Geosci. Remote Sens.,* **28,** 839–845.

Mielke, P. W., 1984: Meteorological applications of permutation techniques based on distance functions. *Handbook of Statistics,* P. R. Krishnaiah and P. K. Sen, Eds., Vol. 4, North Holland, 813–830.

Nadolski, V., 1992: Automated surface observing system user's guide. NOAA Publication 12, 94 pp.

Neale, C. M. U., M. J. McFarland, and K. Chang, 1990: Land-surface-type classification using microwave brightness temperatures from the Special Sensor Microwave/Imager. *IEEE Trans. Geosci. Remote Sens.,* **28,** 829–238.

New, M., M. Hume, and P. D. Jones, 2000: Representing twentieth-century space–time climate variability. Part II: Development of 1901–96 monthly grids of terrestrial surface climate. *J. Climate,* **13,** 2217–2238.

Peterson, T. C., and R. S. Vose, 1997: An overview of the Global Historical Climatology Network temperature database. *Bull. Amer. Meteor. Soc.,* **78,** 2837–2849.

——, A. N. Basist, C. N. Williams, and N. C. Grody, 2000: A blended satellite–in situ near-global surface temperature dataset. *Bull. Amer. Meteor. Soc.,* **81,** 2157–2164.

Prata, A. J., and R. P. Cechet, 1999: An assessment of the accuracy of land surface temperature determination from the GMS-5 VISSR. *Remote Sens. Environ.,* **67,** 1–14.

Prigent, C., W. B. Rossow, E. Matthews, 1997: Microwave land surface emissivities estimated from SSM/I. *J. Geophys. Res.,* **102,** 21 867–21 890.

Quayle, R. G., T. C. Peterson, A. N. Basist, and C. S. Godfrey, 1999: An operational near-real-time global temperature index. *Geophys. Res. Lett.,* **26** (3), 333–335.

Reynolds, R. W., and T. M. Smith, 1994: Improved global sea surface temperature analyses using optimum interpolation. *J. Climate,* **7,** 929–948.

Rosenfeld, S., and N. Grody, 2000: Metamorphic signature of snow revealed in SSM/I measurements. *IEEE Trans. Geosci. Remote Sens.,* **38** (1), 53–63.

Vinnikov, K. Y., A. Robock, S. Qui, J. K. Entin, M. Owe, B. J. Choudhury, S. E. Hollinger, and E. G. Njoku, 1999: Satellite remote sensing of soil moisture in Illinois, United States. *J. Geophys. Res.,* **104,** 4145–4165.

Weng, F., and N. C. Grody, 1998: Physical retrieval of land surface temperature using the Special Sensor Microwave Imager. *J. Geophys. Res.,* **103,** 8839–8848.